

## RADIATIVE COOLING

## Temperature-adaptive radiative coating for all-season household thermal regulation

Kechao Tang<sup>1,2,3†</sup>, Kaichen Dong<sup>1,2†</sup>, Jiachen Li<sup>2,4†</sup>, Madeleine P. Gordon<sup>4,5</sup>, Finnegan G. Reichert<sup>6</sup>, Hyungjin Kim<sup>2,7</sup>, Yoonsoo Rho<sup>8</sup>, Qingjun Wang<sup>1,2</sup>, Chang-Yu Lin<sup>1</sup>, Costas P. Grigoropoulos<sup>8</sup>, Ali Javey<sup>2,7</sup>, Jeffrey J. Urban<sup>5</sup>, Jie Yao<sup>1,2</sup>, Ronnen Levinson<sup>9</sup>, Junqiao Wu<sup>1,2,4\*</sup>

The sky is a natural heat sink that has been extensively used for passive radiative cooling of households. A lot of focus has been on maximizing the radiative cooling power of roof coating in the hot daytime using static, cooling-optimized material properties. However, the resultant overcooling in cold night or winter times exacerbates the heating cost, especially in climates where heating dominates energy consumption. We approached thermal regulation from an all-season perspective by developing a mechanically flexible coating that adapts its thermal emittance to different ambient temperatures. The fabricated temperature-adaptive radiative coating (TARC) optimally absorbs the solar energy and automatically switches thermal emittance from 0.20 for ambient temperatures lower than 15°C to 0.90 for temperatures above 30°C, driven by a photonically amplified metal-insulator transition. Simulations show that this system outperforms existing roof coatings for energy saving in most climates, especially those with substantial seasonal variations.

In countries such as the United States, ~39% of the total energy consumption is in buildings (1). For the residential housing energy portion, ~51% is consumed for heating and cooling to maintain a desirable indoor temperature (~22°C) (2). In contrast to most temperature regulation systems, which require external power input, the mid-infrared (IR) atmospheric transparency window ("sky window") allows thermal radiation exchange between terrestrial surfaces and the 3 K outer space, thus opening a passive avenue for thermal radiative cooling of buildings. This method to cool an outdoor surface such as a roof has been extensively studied in the past (3–6). It is now advanced by the development of daytime radiative cooling (7–13) using materials with low solar absorptance and high thermal emittance in the form of thin films (8), organic paints (10, 14), or structural materials (11).

Past research on daytime radiative cooling, while successful in reducing cooling energy consumption, typically used materials with fixed, cooling-optimized properties, which efficiently emit thermal radiation even when the temperature of the surface is lower than de-

sired, such as during the night or in the winter. This unwanted thermal radiative cooling will increase the energy consumption for heating and may offset the cooling energy saved in hot hours or seasons. This issue is well acknowledged by the research community, and mitigation of the overcooling has become a timely demand (15). To cut the heating penalty from overcooling, a few techniques were recently attempted for switching off thermal radiative cooling at low temperatures (below 22°C). Although effective in switching, these techniques typically require either additional energy input (16, 17) or external activation (18), and in some cases, switching is achieved by mechanical moving parts (19, 20). Developing dynamic structures that automatically cease radiative cooling at low temperatures is therefore highly desirable. Existing efforts in self-switching radiative cooling, however, are either purely theoretical (21–24) or limited to materials characterization with little relevance to practical household thermal regulation (25–28). Very recently, a smart subambient coating was developed (29), focusing on the reduction of solar absorption by fluorescence rather than modulation of thermal emittance by temperature.

We took a different, holistic approach by designing and fabricating a mechanically flexible coating structure to minimize total energy consumption through the entire year. This temperature-adaptive radiative coating (TARC) automatically switches its sky-window emittance to 0.90 from 0.20 when the surface temperature rises above ~22°C, a practical threshold not previously available. Our TARC delivers high radiative cooling power exclusively for the high-temperature condition (Fig. 1A). We also optimized the solar absorptance at ~0.25 (solar reflectance = 0.75) for all-season energy saving in major US cities (fig. S7). Our

TARC demonstrates effective surface temperature modulation in an outdoor test environment. We performed extensive simulations based on the device properties and the climate database, which show advantages of TARC over existing roof coating materials in energy savings for most US cities in different climate zones (Fig. 1C). The energy savings by TARC not only bring economic benefits but also contribute to environmental preservation by reducing greenhouse gas emissions.

We developed the TARC based on the well-known metal-insulator transition (MIT) of the strongly correlated electron materials  $W_xV_{1-x}O_2$  (30–32), and the transition temperature ( $T_{MIT}$ ) is tailored to ~22°C by setting the composition  $x$  at 1.5% (33). We embedded a lithographically patterned two-dimensional array of thin  $W_xV_{1-x}O_2$  blocks in a  $BaF_2$  dielectric layer that sits on top of an Ag film (Fig. 2A). In the insulating (I) state of  $W_xV_{1-x}O_2$  at  $T < T_{MIT}$ , the material is largely transparent to the infrared (IR) radiation in the 8- to 13-μm sky spectral window, so this sky-window IR radiation is reflected by the Ag mirror with little absorption (34). By contrast, the  $W_xV_{1-x}O_2$  becomes highly absorptive in the sky window when it switches to the metallic (M) state at  $T > T_{MIT}$  (34). The absorption is further amplified by the designed photonic resonance with adjacent  $W_xV_{1-x}O_2$  blocks as well as with the bottom Ag layer through the  $\frac{1}{4}$ -wavelength cavity. The  $\frac{1}{4}$ -wavelength cavity structure induces Fabry-Perot resonance and was used in previous work to enhance thermal emission (21, 23). According to Kirchhoff's law of radiation (35), the sky-window emittance equals the sky-window absorptance and switches from low to high when the temperature exceeds  $T_{MIT}$ . Consequently, strong sky-window radiative cooling is turned on in operation exclusively at high temperatures, leaving the system in the solar-heating or keep-warm mode at low temperatures. Details on the fabrication process and structural parameters are found in the supplementary materials (36) (fig. S1).

Our fabricated TARC has high flexibility for versatile surface adaption, as well as a micro-scale structure consistent with the design (Fig. 2B). We examined the emittance switching over the entire sample using a thermal infrared (TIR) camera (Fig. 2C). We imaged the TARC surface together with two reference samples having similar thicknesses but constant low thermal emittance (0.10, copper plate) or constant high thermal emittance (0.95, black tape), respectively. Although the thermal emission of the reference samples appeared to not be strongly temperature sensitive from 20 to 30°C, the TARC showed a marked change, corresponding to the switch in sky-window emittance at the MIT around 22°C.

<sup>1</sup>Department of Materials Science and Engineering, University of California, Berkeley, CA 94720, USA. <sup>2</sup>Materials Sciences Division, Lawrence Berkeley National Laboratory, Berkeley, CA 94720, USA. <sup>3</sup>Key Laboratory of Microelectronic Devices and Circuits (MOE), School of Integrated Circuits, Peking University, Beijing 100871, P. R. China. <sup>4</sup>Applied Science and Technology Graduate Group, University of California, Berkeley, CA, 94720, USA. <sup>5</sup>The Molecular Foundry, Lawrence Berkeley National Laboratory, Berkeley, CA 94720, USA. <sup>6</sup>East Bay Innovation Academy, 3800 Mountain Blvd., Oakland, CA 94619, USA. <sup>7</sup>Department of Electrical Engineering and Computer Sciences, University of California, Berkeley, CA 94720, USA. <sup>8</sup>Department of Mechanical Engineering, University of California, Berkeley, CA 94720, USA. <sup>9</sup>Heat Island Group, Lawrence Berkeley National Laboratory, Berkeley, CA 94720, USA.

\*Corresponding author. Email: wuj@berkeley.edu

†These authors contributed equally to this work.

We measured the spectral properties of the TARC by a UV-visible-NIR spectrometer and Fourier transform infrared spectroscopy (FTIR) for the solar and TIR wavelength regimes, respectively (Fig. 2D). The solar absorptance ( $A$ , 0.3 to 2.5  $\mu\text{m}$ ) is  $\sim 0.25$ , and the sky-window emittance ( $\epsilon_w$ , 8 to 13  $\mu\text{m}$ ) is  $\sim 0.20$  in the I state and  $\sim 0.90$  in the M state, consistent with theoretical simulations and other characterization results (fig. S2 and fig. S3).

The emittance switching of the TARC enables deep modulation of radiative cooling power in response to ambient temperature, which we first measured in vacuum (Fig. 3A). We suspended a heater membrane by thin strings in a vacuum chamber, which was cooled with dry ice to  $\sim -78^\circ\text{C}$  to minimize radiation from the chamber walls. We attached a piece of Al foil with  $\epsilon_{\text{Al}} \approx 0.03$  or a TARC of the same size to the top of the heater in two separate measurements. At each stabilized sample temperature  $T$ , the heating powers needed for the two coating scenarios are denoted as  $P_{\text{Al}}(T)$  and  $P_{\text{TARC}}(T)$ , respectively. The cooling flux (power per area  $A$ ) contributed by the TARC was calculated as  $P''_{\text{cool}}(T) = [P_{\text{TARC}}(T) - P_{\text{Al}}(T)]/A$ . We used the Al foil reference to calibrate background heat loss from thermal conduction through the strings. We plotted the calibrated cooling power (Fig. 3B), which shows an abrupt increase in  $P''_{\text{cool}}(T)$  when  $T$  rises above the MIT temperature.  $P''_{\text{cool}}(T)$  measurements in the I state and M state are well fitted by the Stefan-Boltzmann radiation law, with values of sky-window  $\epsilon_w$  extracted to be  $\sim 0.20$  and  $\sim 0.90$ , respectively, consistent with the spectrally characterized results (Fig. 2D). We considered and corrected the effect of radiation from the chamber wall ( $\sim -78^\circ\text{C}$ ) for the calibration. We introduced a constant factor of  $\gamma$  ( $\approx 0.7$ ) to account for the difference between the vacuum and ambient measurement conditions (details in fig. S4) (36).

We demonstrated the actual outdoor performance of the TARC (Fig. 4). We recorded the surface temperatures ( $T_s$ ) of the TARC, together with a dark roof coating product (Behr no. N520, asphalt gray) and a cool (white) roof coating product (GAF RoofShield white acrylic), over 24 hours on a sunny summer day on a rooftop in Berkeley, California, with a careful design of the measurement system to minimize the effects of artifacts (fig. S5).

From 00:00 to 09:00 local daylight time (LDT), when the ambient temperature was below  $T_{\text{MIT}}$ , the TARC was  $2^\circ\text{C}$  warmer than the two reference roof coatings, arising from the low sky-window emittance ( $\epsilon_w = 0.20$ ) of the TARC in the I state and thus a lower radiative cooling power than the references ( $\epsilon_w = 0.90$ ). The  $2^\circ\text{C}$  temperature elevation is consistent with adiabatic simulation results based on these nominal emittance values and the local

weather database [see the supplementary materials (36), note A, section I]. From 09:00 to 13:00 LDT, when the samples were in direct sunlight,  $T_s$  was dominated by the solar absorption in balance with radiative cooling and air convection, and the differences between the samples agree with the simulated results assuming the solar absorptance  $A$  to be 0.15, 0.25, and 0.70 for the white roof coating, TARC, and the dark roof coating, respectively. After 13:00 LDT, we erected a shield to intentionally block direct solar radiation to the surface of the samples. This imitates the scenario of a cloud blocking the sun but with the rest of the sky mostly clear. We quickly observed a convergence of the  $T_s$  curves for all three samples, an indication that the thermal emittance of the TARC in the M state is close to that of the two references (0.90). This condition persisted for a few hours until  $T_s$  started to drop below  $T_{\text{MIT}} = 22^\circ\text{C}$ . After this point, TARC grew warmer than the two references, with a

final temperature difference of  $\sim 2^\circ\text{C}$ , similar to the 00:00 to 09:00 LDT period. This indicates that the TARC switched to the low-emittance I state. The 24-hour outdoor experiments demonstrate the emittance switching and resultant temperature regulation by TARC. Although the white roof coating shows an advantage over TARC in thermal management in summer daytime and under solar radiation (Fig. 4A), the TARC regulates the roof temperature closer to the heating and cooling setpoints ( $22$  and  $24^\circ\text{C}$ ) than the white roof coating for almost all of the other conditions, including daytime in other seasons and all of the nighttime (fig. S6). From an all-year-round perspective, the TARC demonstrates superiority compared with regular roof coatings in terms of source energy saving.

To directly compare their ambient condition cooling fluxes ( $P''_{\text{cool,amb}}$ ), we heated the TARC and the white roof coating to the air temperature with the direct solar radiation

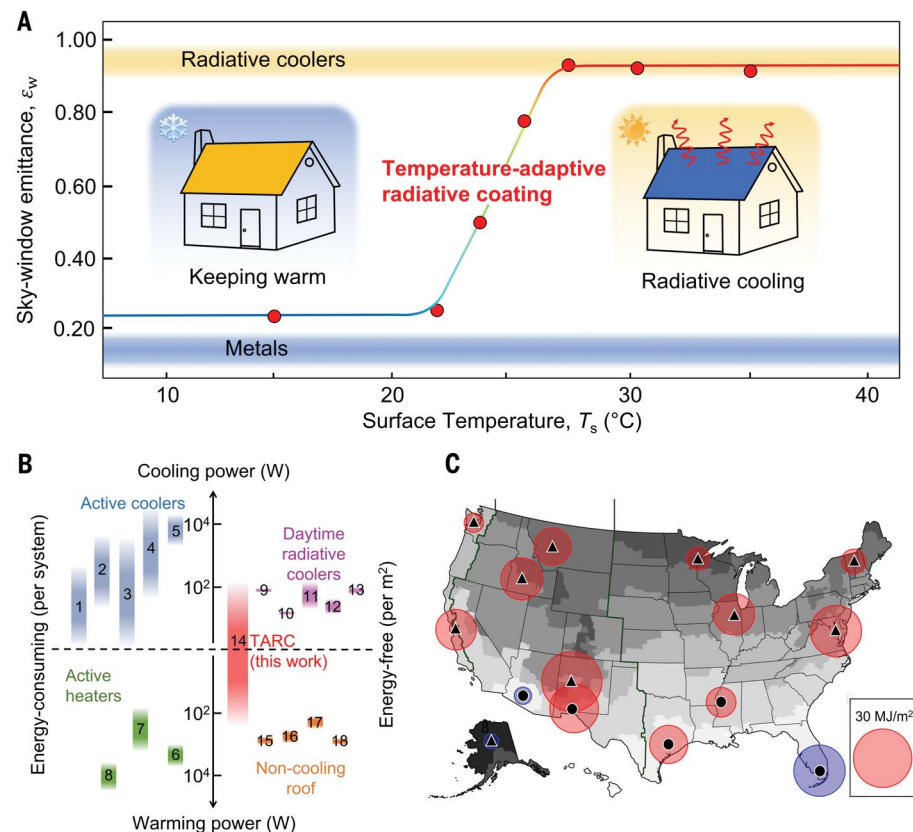


**Fig. 1. TARC and its benefits for household thermal regulation.** (A) Basic property of TARC in sky-window (8 to 13  $\mu\text{m}$ ) emittance modulation and schematics for temperature management when used as a household roof coating. The data points are the measured sky-window emittances of a TARC. The two color bands represent the temperature-independent thermal emittance of metals and radiative coolers. (B) TARC compared with other thermal regulation systems, highlighting the unique benefit of TARC of being simultaneously energy-free and temperature adaptive (details in table S1). (C) SCSEs<sub>min</sub> of TARC compared with other existing roof-coating materials for different cities representing the 15 climate zones in the United States. Red and blue circles indicate positive and negative SCSEs<sub>min</sub> values, respectively. The values are scaled to the area of the circles. Representation of the triangle and circle icons is explained in the materials and methods (subsection, "Projection of energy savings") (36).

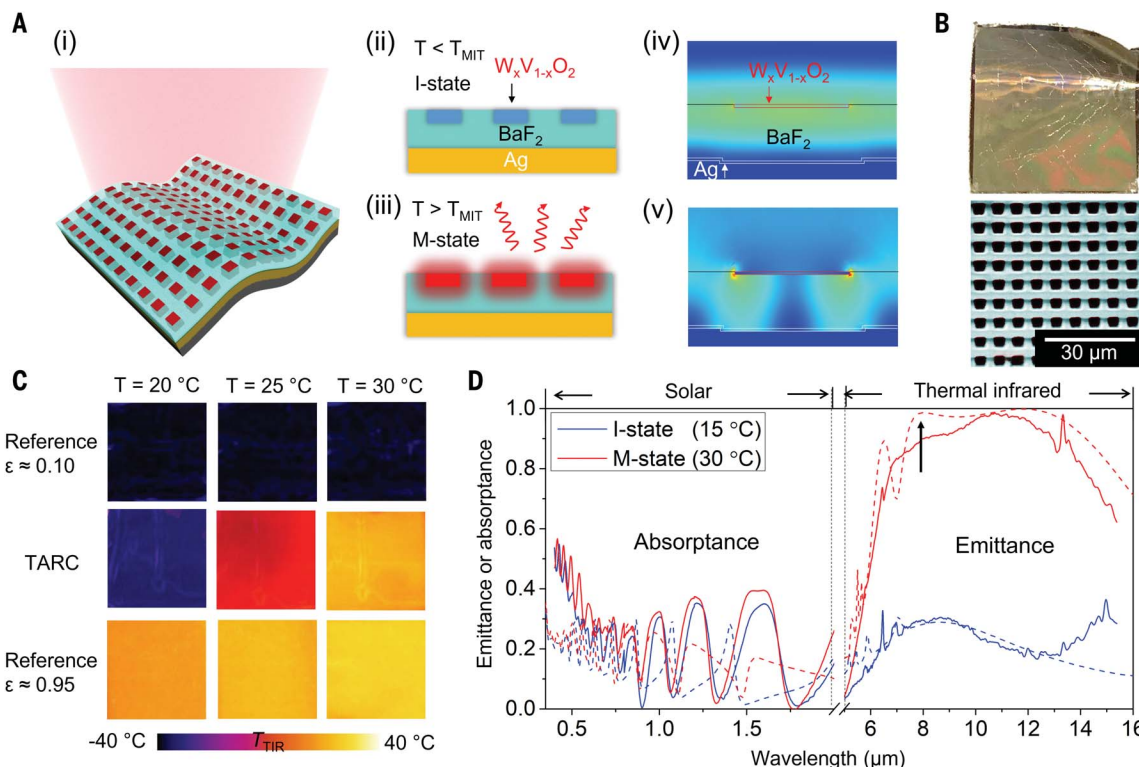


**Fig. 2. Basic properties of TARC with experimental characterization.**

(A) Schematics of the structure (i), materials composition and working mechanism (ii and iii) of the TARC. Subpanels (iv) and (v) show the simulated distribution of electric field intensity below and above the transition temperature, respectively, when electromagnetic waves with a wavelength of 7.8  $\mu\text{m}$  were normally incident on the TARC structure. (B) Photograph (2 cm  $\times$  2 cm) and false-color scanning electron microscope image of TARC showing high flexibility and structural consistency with the design. (C) TIR images of TARC compared with those of two conventional

materials (references) with constantly low or high thermal emittance showing the temperature-adaptive switching in thermal emittance of TARC. (D) Solar spectral absorptance and part of the thermal spectral emittance of TARC at a low temperature and a high temperature, measured by a UV-visible-NIR spectrometer with an integrating sphere and an FTIR spectrometer, respectively. Measurements (solid curves) show consistency with theoretical predictions (dashed curves). The arrow at 7.8  $\mu\text{m}$  denotes the wavelength where the distribution of electric field intensity shown in subpanels (iv) and (v) of (A) are simulated.

blocked.  $P''_{\text{cool,amb}}$  refers to the net cooling flux from the surface—namely, the thermal radiative heat loss flux minus the absorbed diffuse solar irradiance. We plotted the  $P''_{\text{cool,amb}}$  values that we obtained at a low and a high air temperature (Fig. 4B). The TARC exhibits a clear switching of  $P''_{\text{cool,amb}}$  by a factor over five across the MIT. This behavior is in stark contrast to the nearly constant  $P''_{\text{cool,amb}}$  around 120  $\text{W/m}^2$  for the shaded white roof coating, which is consistent with values (90 to 130  $\text{W/m}^2$ ) reported in literature for roofs surfaced with daytime radiative cooling materials (5, 9, 10).

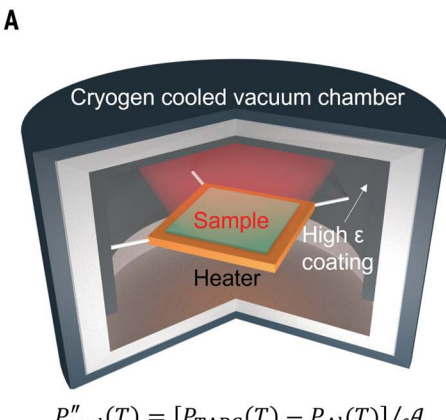
We performed extensive numerical simulations to analyze the performance of TARC in household energy saving for the US cities from an all-season perspective (36). We show the simulated results (Fig. 4C) for Berkeley where the measurements (Fig. 4, A and B) were performed. We calculated an hour-month map of  $T_s$  using a local weather file (37), laying the basis for estimation of energy saving. We assumed heating and cooling setpoints  $T_{\text{set,heat}} = 22^\circ\text{C}$  and  $T_{\text{set,cool}} = 24^\circ\text{C}$  (38), and approx-

imated that the building will need heating when  $T_s < T_{\text{set,heat}}$  and require cooling when  $T_s > T_{\text{set,cool}}$ . We used past simulations of cool-roof energy savings to predict potential space-conditioning source energy savings (SCSES) per unit roof area attainable by using TARC in place of roofing materials that have static values of solar absorptance and thermal emittance (36). The figure of merit of TARC is represented by  $\text{SCSES}_{\text{min}}$ , the minimum value of SCSES found over all existing conventional roofing materials, which have constant values of  $A_{\text{ref}}$  and  $\epsilon_{\text{ref}}$  (Fig. 4C, dashed boxes). We mapped  $\text{SCSES}_{\text{min}}$  for cities representing the 15 US climate zones (Fig. 1C). This figure-of-merit map shows that TARC provides clear, positive annual space-conditioning source energy savings relative to existing roof coating materials in most major cities, except for climates that are constantly cold (such as Fairbanks) or hot (such as Miami) throughout the year. It highlights the advantage of TARC, especially in climate zones with wide temperature variations, day to night or summer to winter. For example, we estimate that for a

single-family home in Baltimore, Maryland, built before 1980, modeled with roof assembly thermal insulation  $4.3 \text{ m}^2/(\text{K}\cdot\text{W})$ , gas furnace annual fuel utilization efficiency 80%, and air conditioner coefficient of performance 2.64 (38),  $\text{SCSES}_{\text{min}}$  is 22.4  $\text{MJ}/(\text{m}^2\cdot\text{y})$ , saving 2.64 GJ/y based on a roof area of 118  $\text{m}^2$ . We also calculated the source energy saving of TARC as a function of its solar absorptance (fig. S7), showing that the actual solar absorptance of TARC is close to the optimal value for major US cities.

The TARC could be readily upgraded for heavy-duty outdoor applications by coating it with a thin polyethylene (PE) membrane, which is nontoxic, hydrophobic, and transparent both in the visible and thermal IR regions. While protecting the TARC from contacting the dust and moisture in complex environments, the PE coating has little impact on the thermal modulation performance (fig. S9). Polymer imprinting instead of photolithography could also be used to more easily produce the material for large scale application. By embedding  $\text{VO}_2$  particles in layered PE

**Fig. 3. Characterization of intrinsic radiative cooling power of TARC in a cryogenic vacuum chamber.** (A) Schematics of the experimental setup showing a thin heater membrane covered by either a TARC or an Al foil and suspended in a cryogen-cooled vacuum chamber. The Al foil reference is used to cancel the effect of thermal loss through conduction. (B) Calibrated experimental cooling flux (power/area) of TARC as a function of temperature in vacuum (the black data line). Fitting of  $P''_{\text{cool}}(T)$  at I and M states by the Stefan-Boltzmann radiation law gives  $\varepsilon_w$  values of 0.20 and 0.90, respectively.



$$P''_{\text{cool}}(T) = [P_{\text{TARC}}(T) - P_{\text{Al}}(T)]/\mathcal{A}$$

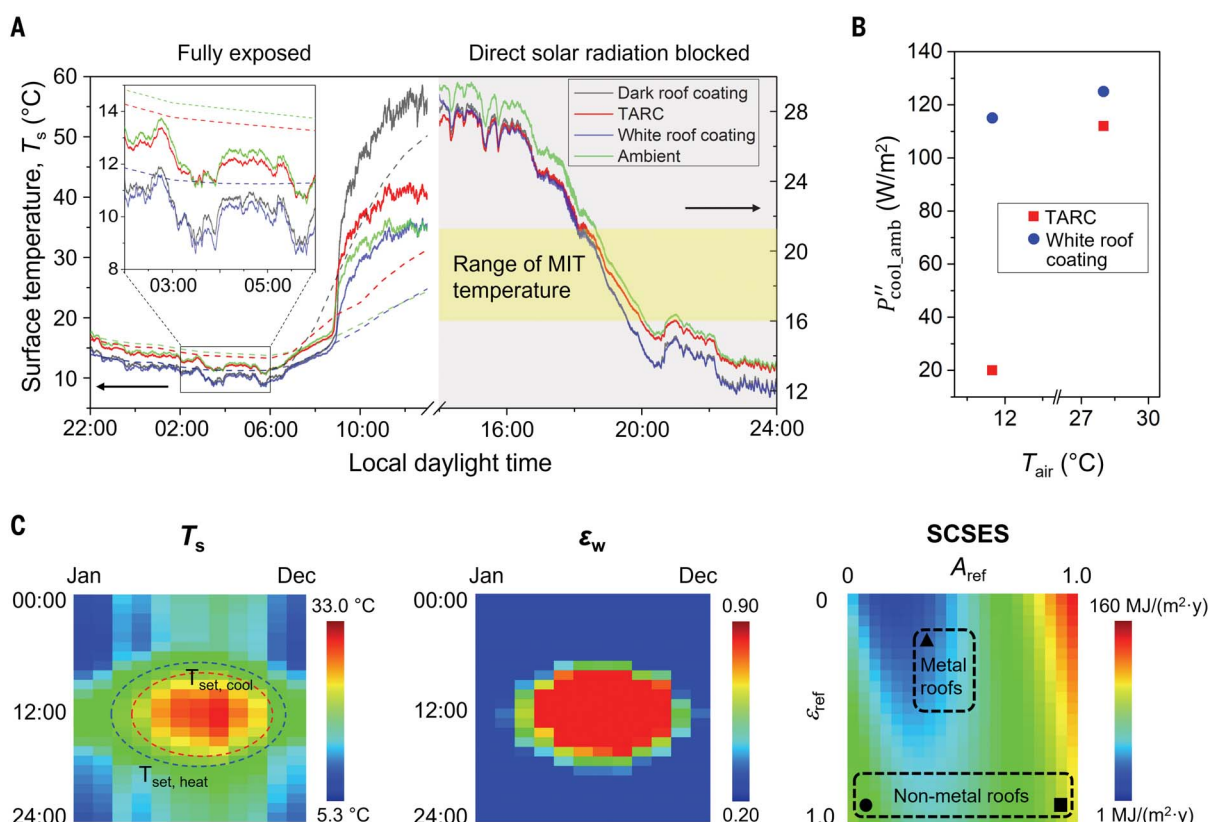
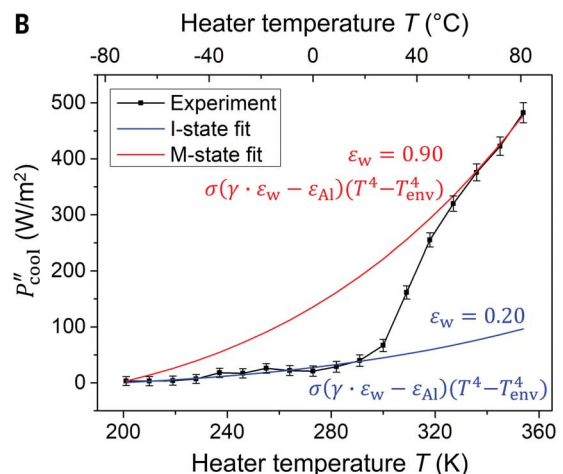


**Fig. 4. Characterization of TARC in an outdoor environment.** (A) Surface temperature of TARC, a commercial dark roof coating ( $A = 0.70$ ,  $\varepsilon_w = 0.90$ ), and a commercial white roof coating ( $A = 0.15$ ,  $\varepsilon_w = 0.90$ ) in an open-space outdoor environment recorded over a day-night cycle. The measurement was taken on 5 July 2020, in Berkeley, California ( $37.91^\circ\text{N}$ ,  $122.28^\circ\text{W}$ ). The solid and dashed curves are experimental data and simulation results based on a local weather database (37), respectively. Measurements starting from 14:00 LDT were performed with the direct solar radiation blocked. Temperature observed after sunset show clear signs

of the TARC shutting off thermal radiative cooling as its surface ambient temperature falls below  $T_{\text{MIT}}$ . (B) Measured ambient cooling power of TARC and white roof coating with direct solar radiation blocked in the outdoor environment. (C)  $T_s$  and the corresponding  $\varepsilon_w$  mapping of TARC over 24 hours and the full year for Berkeley. Also shown are the SCSES of TARC compared with all other materials with fixed solar absorptance ( $A_{\text{ref}}$ ) and fixed thermal emittance ( $\varepsilon_{\text{ref}}$ ). The icons in the SCSES map correspond to those used in Fig. 1C, denoting the radiative parameters ( $A$ ,  $\varepsilon_w$ ) of the strongest rival to TARC in source energy savings for the local climate (36).

membranes, we estimated the multilayered metamaterial to achieve comparable modulation performance ( $\Delta\varepsilon_w > 0.8$ ) as the TARC we presented and would be producible in a roll-to-roll fashion (figs. S10 and S11). Roll-to-

roll manufacturing of PE-based TARC would be beneficial because of its high scalability, low cost (9), and the fact that it is free from the liquid evaporation process in fabrication (39). The PE layer can be also replaced

by other organic or inorganic materials with negligible optical loss in the wavelength ranges of both solar irradiation and IR atmospheric transparency window, so that the TARC technology can be designed specifically

to be endurable in different environmental conditions.

We developed a mechanically flexible, energy-free TARC for intelligent regulation of household temperature. Our system features a thermally driven metal-insulator transition in cooperation with photonic resonance, and demonstrates self-switching in sky-window thermal emittance from 0.20 to 0.90 at a desired temperature of  $\sim 22^\circ\text{C}$ . These attractive properties enable switching of the system from the radiative cooling mode at high temperatures to the solar-heating or keep-warm mode at low temperatures in an outdoor setting. For most cities in the United States, our simulations indicate the TARC may outperform all conventional roof materials in terms of cutting energy consumption for households.

#### REFERENCES AND NOTES

1. US Energy Information Administration, "Annual Energy Review 2020" (2020); <https://www.eia.gov/totalenergy/data/annual/>
2. US Energy Information Administration, "2015 Residential Energy Consumption Survey" (2015); <https://www.eia.gov/consumption/residential/>
3. A. R. Gentle, G. B. Smith, *Adv. Sci. (Weinh.)* **2**, 1500119 (2015).
4. M. Dong, N. Chen, X. Zhao, S. Fan, Z. Chen, *Opt. Express* **27**, 31587–31598 (2019).
5. B. Orel, M. K. Gunde, A. Krainer, *Sol. Energy* **50**, 477–482 (1993).
6. P. Berdahl, M. Martin, F. Sakkal, *Int. J. Heat Mass Transf.* **26**, 871–880 (1983).
7. N. N. Shi *et al.*, *Science* **349**, 298–301 (2015).
8. J. Kou, Z. Jurado, Z. Chen, S. Fan, A. J. Minnich, *ACS Photonics* **4**, 626–630 (2017).
9. Y. Zhai *et al.*, *Science* **355**, 1062–1066 (2017).
10. J. Mandal *et al.*, *Science* **362**, 315–319 (2018).
11. T. Li *et al.*, *Science* **364**, 760–763 (2019).
12. Z. Li, Q. Chen, Y. Song, B. Zhu, J. Zhu, *Adv. Mater. Technol.* **5**, 1901007 (2020).
13. P. Berdahl, *Appl. Opt.* **23**, 370–372 (1984).
14. X. Li *et al.*, *Cell Rep. Phys. Sci.* **1**, 100221 (2020).
15. G. Ulpiani, G. Ranzi, K. W. Shah, J. Feng, M. Santamouris, *Sol. Energy* **209**, 278–301 (2020).
16. K. Goncharov *et al.*, "1500 W deployable radiator with loop heat pipe" (SAE Technical Paper 2001-01-2194, 2001); <https://doi.org/10.4271/2001-01-2194>.
17. C. Lashley, S. Krein, P. Barcomb, "Deployable radiators-A multi-discipline approach" (SAE Technical Paper 981691, 1998); <https://doi.org/10.4271/981691>.
18. H. Zhao, Q. Sun, J. Zhou, X. Deng, J. Cui, *Adv. Mater.* **32**, e2000870 (2020).
19. Z. Xia, Z. Fang, Z. Zhang, K. Shi, Z. Meng, *ACS Appl. Mater. Interfaces* **12**, 27241–27248 (2020).
20. H. Nagano, Y. Nagasaka, A. Ohnishi, *J. Thermophys. Heat Transf.* **20**, 856–864 (2006).
21. M. Ono, K. Chen, W. Li, S. Fan, *Opt. Express* **26**, A777–A787 (2018).
22. M. Chen, A. M. Morsy, M. L. Povinelli, *Opt. Express* **27**, 21787–21793 (2019).
23. S. Taylor, Y. Yang, L. Wang, *J. Quant. Spectrosc. Radiat. Transf.* **197**, 76–83 (2017).
24. W.-W. Zhang, H. Qi, A.-T. Sun, Y.-T. Ren, J.-W. Shi, *Opt. Express* **28**, 20609–20623 (2020).
25. K. Ito, T. Watari, K. Nishikawa, H. Yoshimoto, H. Iizuka, *APL Photonics* **3**, 086101 (2018).
26. K. Nishikawa, K. Yatsugi, Y. Kishida, K. Ito, *Appl. Phys. Lett.* **114**, 211104 (2019).
27. H. Kim *et al.*, *Sci. Rep.* **9**, 11329 (2019).
28. K. Sun *et al.*, *ACS Photonics* **5**, 2280–2286 (2018).
29. X. Xue *et al.*, *Adv. Mater.* **32**, e1906751 (2020).
30. F. J. Morin, *Phys. Rev. Lett.* **3**, 34–36 (1959).
31. T.-L. Wu, L. Whittaker, S. Banerjee, G. Sambandamurthy, *Phys. Rev. B Condens. Matter Mater. Phys.* **83**, 073101 (2011).
32. C. Kim, J. S. Shin, H. Ozaki, *J. Phys. Condens. Matter* **19**, 096007 (2007).
33. S. Lee *et al.*, *Science* **355**, 371–374 (2017).
34. A. S. Barker, H. W. Verleur, H. J. Guggenheim, *Phys. Rev. Lett.* **17**, 1286–1289 (1966).
35. J. Agassi, *Science* **156**, 30–37 (1967).
36. The materials and methods are available as supplementary materials.
37. US Department of Energy, "EnergyPlus Weather Data" (2021); <https://energyplus.net/weather>.
38. P. J. Rosado, R. Levinson, *Energy Build.* **199**, 588–607 (2019).
39. A. Leroy *et al.*, *Sci. Adv.* **5**, eaat9480 (2019).

#### ACKNOWLEDGMENTS

**Funding:** This work was funded by the Office of Science, Office of Basic Energy Sciences, Materials Sciences and Engineering Division, US Department of Energy, under contract no. DE-AC02-05-CH11231 (EMAT program KC1201). Work at the Molecular Foundry was supported by the Office of Science, Office of Basic Energy Sciences, US Department of Energy, under contract no. DE-AC02-05CH11231. J.W. acknowledges support from a Bakar Prize. R.L. acknowledges support from the Assistant Secretary for Energy Efficiency and Renewable Energy, Building Technologies Office, of the US Department of Energy under contract no. DE-AC02-05CH11231. J.Y. acknowledges support from the National Science Foundation under grant no. 1555336. M.P.G. gratefully acknowledges the National Science Foundation for fellowship support under the National Science Foundation Graduate Research Fellowship Program. **Author contributions:** K.T., K.D., J.L., and J.W. conceived the general idea. K.T. and K.D. designed the device. K.T. fabricated the device. K.T., M.P.G., H.K., Q.W., A.J., J.J.U., and J.Y. contributed to the spectral characterizations. K.T., K.D., J.L., Y.R., and C.P.G. contributed to the solar simulator characterizations. K.T., J.L., and C.-Y.L. performed the vacuum chamber characterizations. K.T., K.D., J.L., and J.W. performed the field experiments. K.D., J.L. and J.Y. performed the numerical electromagnetic simulations. K.T., F.G.R., and R.L. performed all other simulations. All authors discussed and analyzed the results. K.T., K.D., J.L., and J.W. wrote the manuscript with assistance from other authors. All authors reviewed and revised the manuscript.

**Competing interests:** R.L. is an unpaid, nonvoting member of the board of directors of the Cool Roof Rating Council (CRRC) and a paid consultant to the CRRC. K.T., K.D., J.L., and J.W. are inventors of a provisional patent application related to this work. The authors declare that they have no competing interests. **Data and materials availability:** All data required to evaluate the conclusions in the manuscript are available in the main text or the supplementary materials.

#### SUPPLEMENTARY MATERIALS

[science.org/doi/10.1126/science.abf7136](https://science.org/doi/10.1126/science.abf7136)

Nomenclature

Materials and Methods

Supplementary Text

Figs. S1 to S19

Tables S1 to S6

References (40–105)

13 November 2020; resubmitted 5 May 2021

Accepted 26 October 2021

[10.1126/science.abf7136](https://science.org/doi/10.1126/science.abf7136)